Journal of Colloid and Interface Science 547 (2019) 102–110

Contents lists available at ScienceDirect

Journal of Colloid and Interface Science

journal homepage: www.elsevier.com/locate/jcis

Highly efficient ethylene glycol electrocatalytic oxidation based on bimetallic PtNi on 2D molybdenum disulfide/reduced graphene oxide nanosheets

Hongmin Zhang [a], Chunyang Zhai [a,*], Haifeng Gao [a], Nianqing Fu [c,*], Mingshan Zhu [a,b,*]

[a] School of Materials Science and Chemical Engineering, Ningbo University, Ningbo 315211, PR China
[b] School of Environment, Jinan University, Guangzhou 510632, PR China
[c] School of Materials Science and Engineering, South China University of Technology, Guangzhou 510640, PR China

GRAPHICAL ABSTRACT

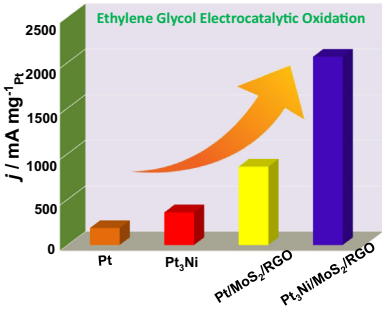

ARTICLE INFO

Article history:
Received 21 February 2019
Revised 25 March 2019
Accepted 27 March 2019
Available online 28 March 2019

Keywords:
Direct ethylene glycol fuel cell
Pt_xNi alloy
Molybdenum disulfide
Reduced graphene oxide
Ethylene glycol oxidation reaction

ABSTRACT

In this paper, a two-dimensional (2D) hybrid material of molybdenum disulfide (MoS_2)/reduced graphene oxide (RGO) is facilely synthesized and used as an ideal support for the deposition of Pt nanoparticles. The as-prepared Pt/MoS_2/RGO composites are further worked as electrocatalysts towards ethylene glycol oxidation reaction (EGOR). In addition, when alloying with Ni, the composite shows obvious enhancement in electrocatalytic performance for EGOR. Specifically, the optimized molar ratio of Pt to Ni is 3:1, namely Pt_3Ni/MoS_2/RGO performs the strongest current density of 2062 mA mg_{Pt}^{-1}, which is 11.1, 5.80 and 2.40 times higher than those of Pt, Pt_3Ni and Pt/MoS_2/RGO electrodes, respectively. The systematically electrochemical measurements indicate that the largely promoted electrocatalytic performances of Pt_3Ni/MoS_2/RGO are mainly attributed to the synergistic effect of Ni and Pt, and 2D sheets of MoS_2/RGO. This excellent performance indicates that the reported electrocatalytic material could be an efficient catalyst for the application in direct ethylene glycol fuel cell and beyond.

1. Introduction

The reserves of fossil fuel are quickly depleted and world may have an energy crisis in the end [1]. It has been known that heavily relying on fossil fuel is harmful to environmental. It is urgent to search a new way to solve the current energy crisis, such as finding a feasible alternative fuel sources and exploring new energy

* Corresponding authors at: School of Materials Science and Chemical Engineering, Ningbo University, Ningbo 315211, PR China (M.Zhu).
E-mail addresses: zhaichunyang@nbu.edu.cn (C. Zhai), msnqfu@scut.edu.cn (N. Fu), mingshanzhu@yahoo.com (M. Zhu).

https://doi.org/10.1016/j.jcis.2019.03.090
0021-9797/

conversion devices [1–3]. So far many new forms of clean energy, such as solar energy, water splitting, air batteries, and so on [4–7] has been extensively studied. Fuel cell, with the features of beneficial energy efficiency, high specific energy/power densities and low even zero emissions, has been generally regarded as an useful electrochemical technology for energy storage and conversion [3,8–10].

In liquid fuel cell application, ethylene glycol (EG) is safer than the other alcohols due to the fact that EG has lower toxicity, higher ignition point (418 °C) and boiling point (198 °C) [10–12]. Moreover, EG is not categorized as flammable, which makes it air shippable [13]. Meanwhile, the complete oxidation of EG delivers $10e^-$ compared with $6e^-$ by methanol [14]. The theoretical power capacity of EG is provided about 4.8 Ah mL^{-1}, which is much higher than methanol (4 Ah mL^{-1}) [15]. In addition to its high capacity, EG has a superiority of high volumetric energy density. Furthermore, EG could be produced from catalytic conversion of fibrin with high output, and fibrin is the most abundant biomass-related resource in nature, which means EG can be considered as a renewable fuel [16–18]. Therefore, direct ethylene glycol fuel cells (DEGFCs) have a greater advantage in practical application [10–18].

Two-dimensional (2D) materials have attracted a huge interest in recent years. Graphene, as the most typical 2D material, owing to its super-high specific surface area, outstanding electrical conductivity and remarkable chemical stability [19–21], has been certified as a hopeful Pt-based electrocatalyst support. With similar structures as graphene, 2D nanomaterial of molybdenum disulfide (MoS_2) has drawn attentions to scientists as well [22–24]. For example, Du and Zhu's group [24] reported a facile method to synthesize composites of molybdenum disulfide/reduced graphene oxide (MoS_2/RGO), which Pt nanoparticles can be dispersed well on their surfaces. Finally, Pt/MoS_2/RGO composites displayed the 5.65 times higher eletrocatalytic methanol oxidation activity compared with commercial Pt/C species. However, to construct more methods to face the high demand for energy is still needed.

Over the past two decades, different kinds of Pt-based alloy catalysts have been tested [25–27]. Pt-based alloy system has shown higher electrocatalyst activity and better stability than single component alone. Therefore, some inexpensive metals like Ni, Co, Cu, *etc.* were introduced into Pt catalysts to promote ethylene glycol oxidation reaction (EGOR) through synergistic and electronic effects [28–32]. The modified Pt catalysts can decrease the usage of Pt, therefore, lower the catalyst cost for DEGFCs. By the way, electronic structure of Pt atom on the bi-metallic alloys can be adjusted by these promoters [28–32].

Herein, we reported the synthesis of Pt-based composite EGOR catalyst by using MoS_2/RGO as electrocatalyst support materials. Simultaneously, Ni was added into the Pt system, resulting in Pt_xNi/MoS_2/RGO nanocomposites and finally used in EGOR. Different Ni doping level was investigated, and the optimum electrode of Pt_3Ni/MoS_2/RGO showed 5.80 and 2.40 times higher than those of Pt_3Ni and Pt/MoS_2/RGO electrodes, respectively. At the same time, the long-term stability of Pt_xNi/MoS_2/RGO electrode also showed steadier than the other electrodes. The alloying with Ni results in the low Pt usage, as well as the high catalytic performance and stability. The present result suggests that Pt_xNi/MoS_2/RGO could be used as a prospective electrocatalyst for the application in fuel cells.

2. Experimental section

2.1. Materials and characterization

Heptamolybdate tetrahydrate ($(NH_4)_6Mo_7O_{24}{\cdot}4H_2O$), thiourea ($CH_4N_2S$), chloroplatinic acid ($H_2PtCl_6{\cdot}6H_2O$), nickelnitrate (Ni $(NO_3)_2{\cdot}6H_2O$), ethylene glycol ($(CH_2OH)_2$, EG), ethanol (CH_3CH_2OH) and potassium hydroxide (KOH) are obtained from Sinopharm Chemical Reagent Co., Ltd. without further purification before use. All of the chemical reagents are of analytical grade. Graphene oxide solution (GO, XF002-1) is received from Nanjing XFNANO Materials Tech Co., Ltd. Deionized water (DI) is used during the electrochemical experiment.

2.2. Synthesis of MoS_2/RGO nanosheets

The MoS_2/RGO nanosheets were synthesized by a simple hydrothermal method. Generally, 0.177 g $(NH_4)_6Mo_7O_{24}{\cdot}4H_2O$ (1 mmol) and 0.38 g CH_4N_2S (5 mmol) and 5 mL GO solution (0.008 g) were dispersed in 15 mL water under ultrasonication for 1 h. Then the homogeneous solution was transferred into a 25 mL Teflon autoclave and held at 210 °C for 24 h. After the mixture was cooled to room temperature naturally, the precipitates were collected by centrifugation and washed with water and ethanol three times, respectively, subsequently dried in a vacuum oven at 60 °C overnight, resulting in the black powder.

2.3. Synthesis of Pt_xNi/MoS_2/RGO and Pt/MoS_2/RGO nanocomposites

The PtNi/MoS_2/RGO nanocomposites were synthesized by a solvothermal method. Generally, 30 mg as-synthesized MoS_2/RGO nanosheets, 8.6 mg $Ni(NO_3)_2{\cdot}6H_2O$ and 0.78 mL H_2PtCl_6 (0.038 M) solution were added into 15 mL DMF under ultrasonication for 0.5 h. Then the homogeneous solution was transferred into a 25 mL Teflon autoclave and held at 160 °C for 6 h. After that, the precipitates were collected by high-speed centrifugation and washed with water and ethanol three times, respectively, and then dried in a vacuum oven at 40 °C for 12 h, resulting in PtNi loading on MoS_2/RGO nanosheets. The catalysts prepared are denoted as Pt_2Ni/MoS_2/RGO, Pt_3Ni/MoS_2/RGO and Pt_4Ni/MoS_2/RGO based on the mole ratio of Pt to Ni. All the catalysts contained a total metal loading of 20 wt%. For comparison, Pt/MoS_2/RGO nanocomposites were prepared without Ni precursor, and the Pt_3Ni samples were prepared in the absence of MoS_2/RGO nanosheets.

2.4. Preparation of working electrode

The working electrode was prepared through depositing as-prepared samples on the surface of pre-polished glassy carbon electrode (GCE, 3 mm in diameter) Typically, 2 mg as-prepared Pt_3Ni/MoS_2/RGO powder was dispersed in 1 mL water/ethanol mixtures and 20 μL Nafion (Dupond, USA) under ultrasonication condition, then 5 μL of the homogeneous suspension was deposited on a pre-polished GCE surface and dried at room temperature, resulting in Pt_3Ni/MoS_2/RGO modified GCE electrode.

2.5. Electrochemical measurements

The electrochemical characterization was carried in a CHI 660E electrochemical workstation (Shanghai Chenhua Instrumental Co., Ltd.). A conventional three electrodes system was used with sample modified GCE, Pt wire and silver-silver chloride electrode (Ag/AgCl) as the working, counter and reference electrode, respectively. All potentials were referred in this paper with respect to Ag/AgCl electrode. The all electrochemical measurements were performed in 1.0 M EG + 1.0 M KOH solution at room temperature. Cyclic voltammetries (CVs) were conducted at the potential range from −0.7 V to 0.4 V (vs. Ag/AgCl) with the scan rate at 50 mV s^{-1}. The chronoamperometry (CA) and chronopotentiometry (CP) tests were carried out at −0.2 V for 1500 s and 100 μA, respectively. Electrochemical impedance spectroscopy (EIS) measurements

were implemented under an AC perturbation signal of 5.0 mV over the frequency range from 1 Hz to 100 kHz at −0.25 V.

2.6. Characterizations

The morphologies of the samples were characterized by scanning electron microscope (SEM, Nava NanoSEM 450) and transmission electron microscopy (TEM, JEM-2100F). The energy dispersive X-ray (EDX) equipped to Nava NanoSEM 450. X-ray diffraction (XRD) patterns of the samples were obtained from PANalytical X' Pert PRO MRD system. X-ray photoelectron spectroscopy (XPS) was recorded by an ESCALab220i-XL electron spectrometer. Thermogravimetric analyse (TGA) was measured by TG/DTA 7300.

3. Results and discussion

The MoS_2/RGO nanocomposites were easily obtained by a simple hydrothermal method. During the process, CH_4N_2S was used as S resource and reductant. The GO was reduced to RGO as well as $(NH_4)_6Mo_7O_{24}$ was converted to well-crystallized MoS_2 on RGO nanosheets after reaction. Pt_xNi/MoS_2/RGO composites were obtained by solvothermal method. The morphologies of MoS_2/RGO and Pt_3Ni/MoS_2/RGO nanocomposites were characterized by SEM measurement firstly. The 2D typical flower-like structures assembled by nanosheets were observed in MoS_2/RGO and Pt_3Ni/MoS_2/RGO nanocomposites, as shown in Fig. 1A and B. Fig. 1B shows that Pt_3Ni nanoparticles were dispersed on the surface of MoS_2/RGO well. The TEM image of MoS_2/RGO is shown in Fig. 1C, which clearly indicated that the MoS_2 nanosheets were tightly laid flat on the RGO sheets. Fig. 1D shows that Pt_3Ni nanoparticles were deposited on the surface of MoS_2/RGO well. In addition, the average diameter of Pt_3Ni nanoparticles on the surface of MoS_2/RGO sheets is about 5.8 nm. It can be observed high definition crystal fringes from HRTEM image of Pt_3Ni/MoS_2/RGO in Fig. 1E. The estimated lattice spacing was 0.19 nm, referring to (2 0 0) crystal plane (0.19 nm) of Pt_3Ni, which is slightly less than Pt (2 0 0) spacing (0.196 nm, JCPDS-04-0802).

The crystal structures of the as-prepared samples were further tested by XRD. As shown in Fig. 2A, all samples exhibit two strong diffraction peaks at 13.7° and 33.4°, which are recognized as to the diffraction from (0 0 2) and (1 0 1) planes of MoS_2, respectively [24,33]. For RGO based samples, it is difficult to observe characteristic peak of graphene (at about 26.6°), possibly due to the small quanity of RGO (about 5 wt%) [34]. In the XRD pattern of Pt/MoS_2/RGO nanocomposite, three peaks at 39.7°, 46.2° and 67.4° corresponds (1 1 1), (2 0 0) and (3 1 1) of Pt plane, respectively. However, for Ni/MoS_2/RGO nanocomposite, there are no significant characteristic peaks of Ni, which is due to its small content and poor crystallinity. For Pt_3Ni/MoS_2/RGO, three diffraction peaks locates at 40.0°, 46.5° and 68.4° are recognized as (1 1 1), (2 0 0) and (2 2 0) planes, respectively [28,35,36]. It's found that these peaks are slight shift compare to pure Pt, indicating the alloying of Pt with Ni. This phenomenon is match well with above HRTEM analysis.

Meanwhile, the composition of Pt_3Ni/MoS_2/RGO nanocomposite was investigated by STEM-EDX spectrum shown in Fig. 2B and C. Firstly, the STEM image (Fig. 2B) indicates that PtNi nanoparticles were deposited and uniformly distributed on the surface of MoS_2/RGO. Then, the EDX spectrum of Pt_3Ni/MoS_2/RGO (Fig. 2C) shows that all five elements were successfully confirmed in the composites. At the same time, the corresponding EDX elemental mapping images of Pt_3Ni/MoS_2/RGO were shown in Fig. 2D–H. The intense signals of C, Mo and S correspond to the MoS_2/RGO based-support, indicating the successful construction of 2D MoS_2/RGO composites. Moreover, the signals of Ni and Pt were captured well, suggesting that Pt and Ni nanoparticles were compounded on MoS_2/RGO.

Thermogravimetric (TG) measurement for the Pt_3Ni/MoS_2/RGO nanocomposite was carried out. As shown in Fig. 3, the mass loss of sample from room temperature to 100 °C is about 12%, which was due to the adsorbed water in sample. Additionally, a distinct mass loss between 200 and 500 °C for Pt_3Ni/MoS_2/RGO was attributed to the removal of oxygen functional groups. Finally, the Pt_3Ni/MoS_2/RGO nanocomposites contained about 70 wt% of Pt_3Ni/MoS_2 nanocrystals [37,38].

XPS was performed to investigate the surface chemical composition and the oxidation state of the Pt/MoS_2/RGO and Pt_3Ni/MoS_2/RGO nanocomposites. As shown in Fig. 4A, two well doublet peaks

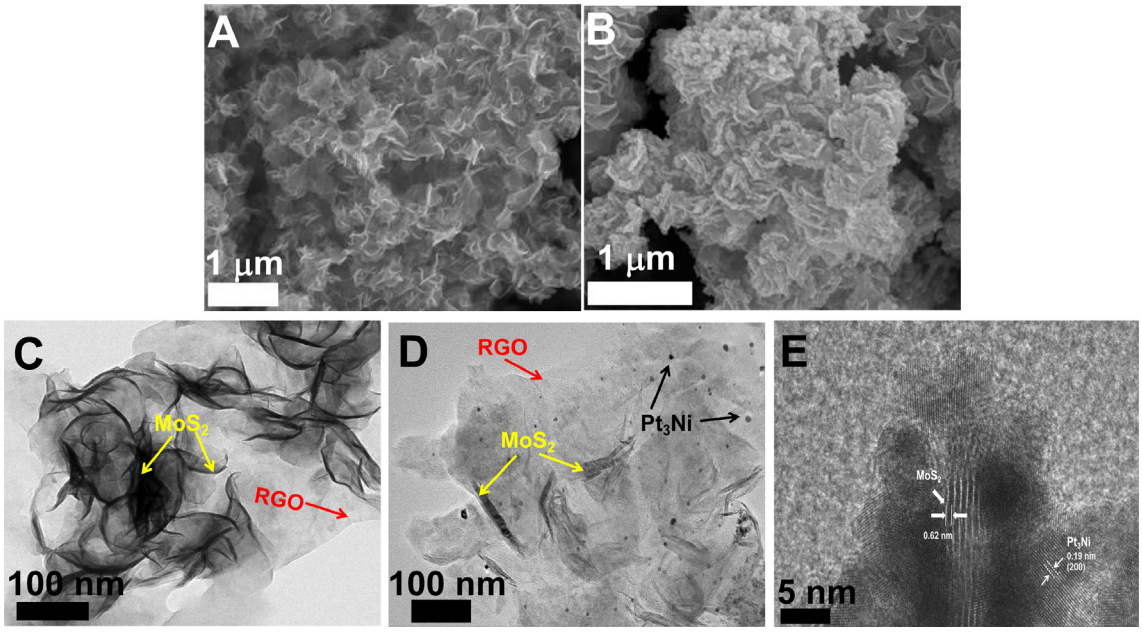

Fig. 1. SEM images of MoS_2/RGO (A) and Pt_3Ni/MoS_2/RGO (B) nanocomposites. TEM images of MoS_2/RGO (C) and Pt_3Ni/MoS_2/RGO (D) nanocomposites. HRTEM image of Pt_3Ni/MoS_2/RGO (E).

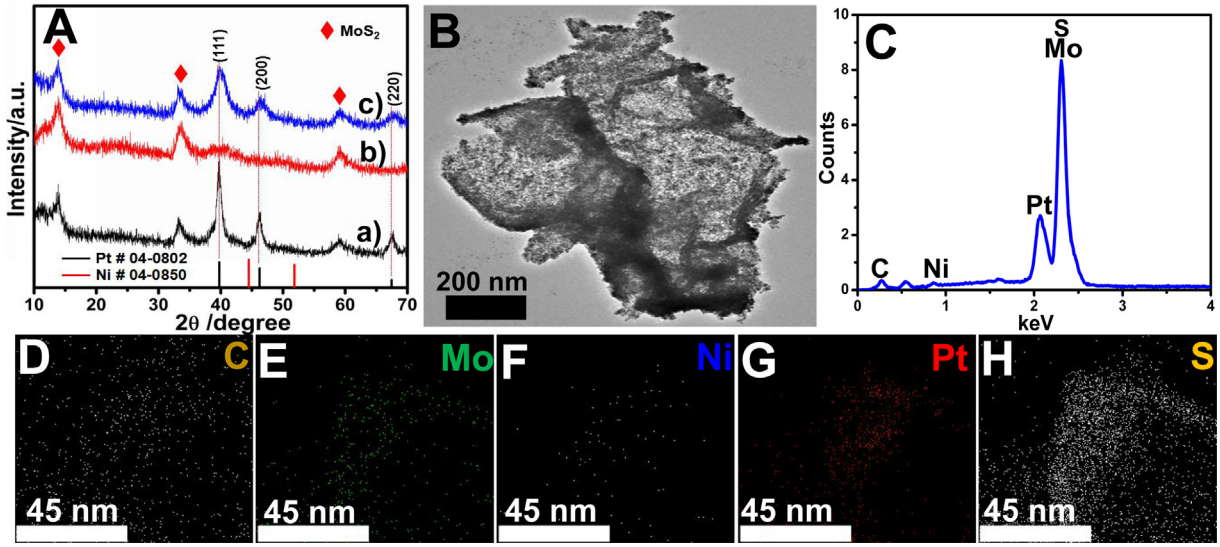

Fig. 2. XRD patterns (A) of Pt/MoS_2/RGO (a), Ni/MoS_2/RGO (b), and Pt_3Ni/MoS_2/RGO (c). Low-magnification HAADF-STEM (B) image and EDX (C) and corresponding EDX elemental mapping of C (D), Mo (E), Ni (F), Pt (G), S (H) elements in the Pt_3Ni/MoS_2/RGO.

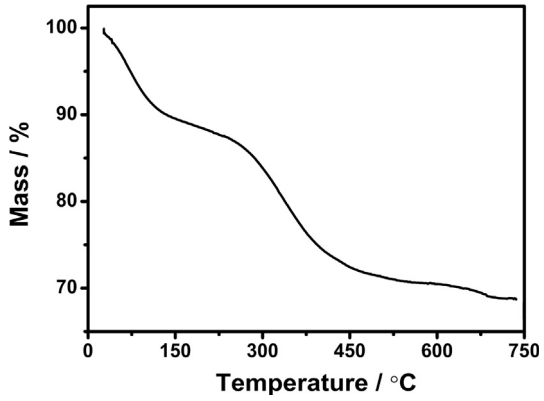

Fig. 3. TG curve of Pt_3Ni/MoS_2/RGO nanocomposites.

at 228.9 and 232.2 eV corresponds to Mo $3d_{5/2}$ and Mo $3d_{3/2}$, respectively, which is attributed to Mo^{4+} in MoS_2 [33,39]. Meanwhile, an obvious peak located at 226.6 eV corresponds to S 2s is observed in the Mo 3d spectra. The peaks located at 161.7 and 162.9 eV in Fig. 4B attribute to the binding energy for S $2p_{3/2}$ and S $2p_{1/2}$, respectively [33,39]. From Fig. 4C and D, the peaks at 286.2 eV and 533.8 eV correspond to C 1s and O 1s, respectively. A typical high resolution XPS spectrum of Pt 4f of Pt/MoS_2/RGO is shown in Fig. 4E. Two peaks originating from the spin orbital splitting of the $4f_{7/2}$ and $4f_{5/2}$ states locate at the binding energies of 73.1 and 76.2 eV, respectively. Moreover, the binding energy of Pt_3Ni/MoS_2/RGO catalyst slight shifts to higher level compared with that of Pt/MoS_2/RGO owing to the interaction between Pt and Ni. The Ni 2p XPS spectrum of the Pt_3Ni/MoS_2/RGO is shown in Fig. 4F. Fitting the curve of Ni 2p signal, it provides different Ni species was deduced, including $Ni(OH)_2$ and NiOOH, with Ni $2p_{3/2}$ peaks with binding energy of 856.2 eV and 857.2 eV, respectively [40–42].

In order to examine the electrocatalytic activity of these different samples, the CVs of ethylene glycol electrooxidation were measured in 1.0 M EG + 1.0 M KOH solution and the results are shown in Fig. 5. Firstly, the electrodes did not show any redox chemistry in 1.0 M KOH solution in the absence of EG. Secondly, all CV curves contain two oxidation peaks in the presence of EG, suggesting the effective of oxidation of EG. The first oxidation peak located in the forward scan corresponds to EG adsorption oxidation, while the next oxidation peak in the negative scan is ascribed to further oxidation from newly produced intermediates from the forward scan. The current density of Pt and Pt_3Ni electrodes are 186 and 357 mA mg_{Pt}^{-1}, respectively. After deposition of Pt nanoparticles on the surface of MoS_2/RGO nanosheets, the CV of Pt/MoS_2/RGO electrode shows the lager peak of 858 mA mg_{Pt}^{-1}. Furthermore, when the Pt_3Ni nanoparticles were deposited on the surface of MoS_2/RGO nanosheets, the current peak density of Pt_3Ni/MoS_2/RGO electrode was further increased to 2062 mA mg_{Pt}^{-1}, which is 11.1, 5.80, 4.30, 4.68 and 2.40 times higher than Pt, Pt_3Ni, Pt_3Ni/RGO, Pt_3Ni/MoS_2 and Pt/MoS_2/RGO electrodes, respectively. At the same time, the effect of different molar ratio of Pt and Ni on the catalytic performance of ethylene glycol electrooxidation was carried out. From Fig. 5B, it obviously shows that the Pt_3Ni/MoS_2/RGO sample reveals the best electrocatalytic activity. The data for EGOR on different electrode were normalized by surface area (0.07 cm^2) and summarized in Table 1.

These results demonstrate that the excellent electrocatalytic performances of Pt_3Ni/MoS_2/RGO composites. Compare to bare Pt or Pt_3Ni, the introduction of MoS_2 and RGO can improve the catalytic activities obviously. This is contributed to the well-dispersion of electrocatalyst on the surface of 2D nanosheets of MoS_2 and RGO, and high electronic transport property of RGO. Secondly, after Ni was introduced in the bimetallic PtNi, the Ni can adjust the electronic structures of Pt or it acts as electron donation to Pt in PtNi alloy, resulting in a decrease of Pt 4f binding energy [28]. Moreover, the generation of Ni hydroxide passivated surface of the PtNi catalyst, which contributes to the relatively stable activity [43]. However, the overload amount of Ni would result in some Pt surface active sites covered by Ni species, leading to the decreased activity of catalyst. We also take the catalyst electrocatalytic activity to compare with the other materials. The results are shown in Table 2. Thus, these features imply the most efficient electrooxidation of EG by using Pt_3Ni/MoS_2/RGO among the tested catalysts.

To further evaluate the interface charge mobility of electrode, the electrochemical impedance spectroscopies (EIS) at different potential range of Pt_3Ni/MoS_2/RGO modified electrode in the 1.0 M EG + 1.0 M KOH solution were studied (Fig. 6A–C). When the potential continuously increased from −0.60 V to −0.30 V

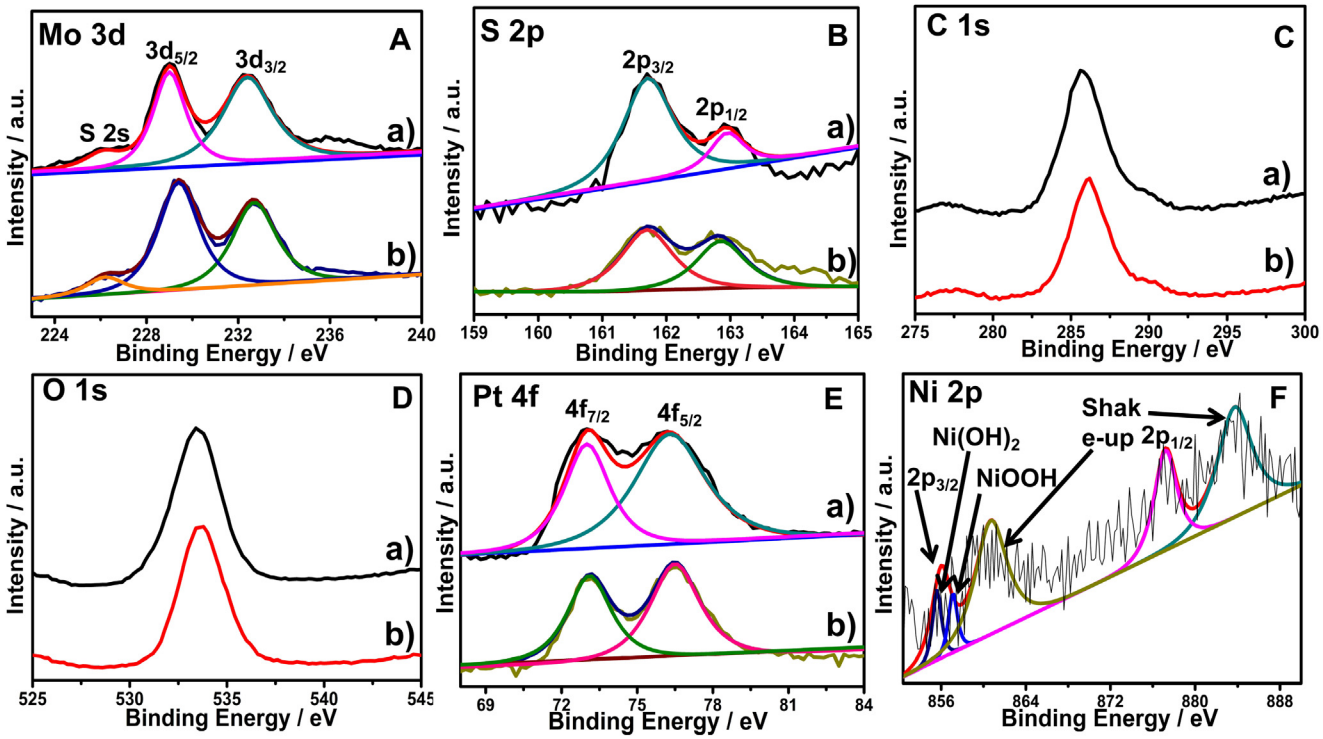

Fig. 4. XPS spectra of Mo 3d (A), S 2p (B), C 1s (C), O 1s (D), and Pt 4f (E) of $Pt/MoS_2/RGO$ (a) and $Pt_3Ni/MoS_2/RGO$ (b) nanocomposites. XPS spectrum of the Ni 2p (F) in the $Pt_3Ni/MoS_2/RGO$ nanocomposites.

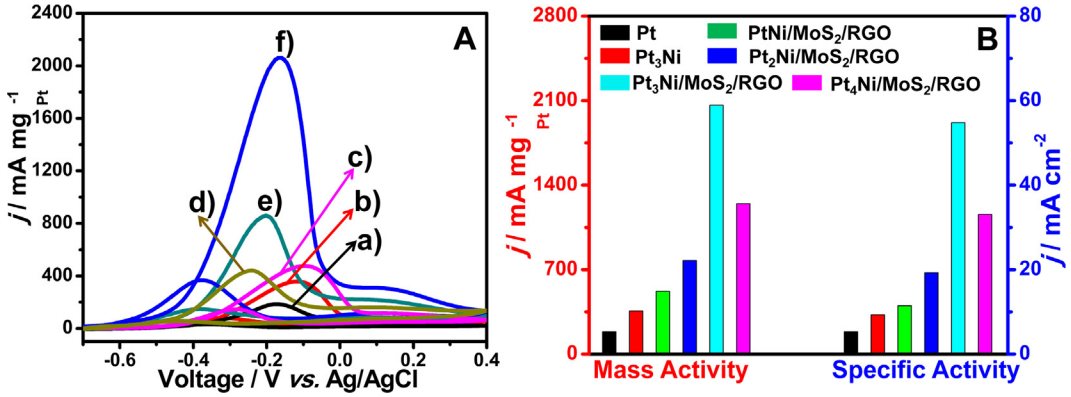

Fig. 5. (A) The 100th CVs of Pt (a), Pt_3Ni (b), Pt_3Ni/RGO (c), Pt_3Ni/MoS_2 (d), $Pt/MoS_2/RGO$ (e), and $Pt_3Ni/MoS_2/RGO$ (f) electrodes in 1.0 M EG + 1.0 M KOH solution at a scan rate of 50 mV s^{-1}. (B) Histogram of different electrodes activities in 1.0 M EG + 1.0 M KOH solution.

Table 1
The summary data of current densities on different electrode for EGOR.

Electrode	Pt	Pt_3Ni	Pt_3Ni/RGO	$Pt/MoS_2/RGO$	$PtNi/MoS_2/RGO$	$Pt_2Ni/MoS_2/RGO$	$Pt_3Ni/MoS_2/RGO$	$Pt_4Ni/MoS_2/RGO$
j/mA mg_{Pt}^{-1}	186	357	476	858	521	776	2062	1245
j/mA cm^{-2}	2.60	9.30	12.4	24.5	11.5	19.3	54.8	33.1

(Fig. 6A), the diameters of the impedance arcs (DIA) decreased clearly. This is because the CO intermediate species produced from EG dehydrogenation were removed at a higher potential, releasing more active sites for EGOR [35]. As shown in Fig. 6B, with the potential increasing from −0.30 V to −0.15 V, the DIA is the smallest at the potential of −0.25 V. The result means that the $Pt_3Ni/MoS_2/RGO$ modified electrode has the better electron transfer performance at this potential. When the potential further increased from −0.15 V to 0 V (Fig. 6C), the DIA begin to increase and reverse to the second quadrant at −0.10 V. This behavior is due to the oxidation removal of CO-like intermediate from the catalyst surface, which leads to the restoration of the catalytic active sites. At 0 V and −0.05 V, the Nyquist plots are similar to the condition occurs at −0.1 V. Moreover, the EIS of different modified electrodes were investigated (Fig. 6D) and compared by the equivalent circuits (inset in Fig. 6D), which is used to fit the EIS spectra to exhibit the parameter of charge transfer resistance, where R_s and R_{ct} are represented as the electrolyte resistance and charge-transfer

Table 2
Recent reports on electrocatalytic activity of ethylene glycol oxidation by using different materials.

Electrocatalyst	Electrocatalytic performance	Reference
Pt_2Ni_1/C	204 mA mg^{-1}	[43]
PtPd@Pt NCs/rGO	230 mA mg^{-1}	[44]
Pt-Pd nanoflowers	1720 mA mg^{-1}	[45]
Snowflake-like PdAu	1990 mA mg^{-1}	[46]
Pt@Pd NCs	688.1 mA mg^{-1}	[47]
Pd–Ag/C nanoparticle	956 mA mg^{-1}	[48]
Pd/Ag@C	1027 mA mg^{-1}	[49]
Au–Pd@Pd nanocrystals	535.4 mA mg^{-1}	[50]
PtAg NCs	863 mA mg^{-1}	[31]
$Pt_3Ni/MoS_2/RGO$	2062 mA mg^{-1}	This work

resistance at electrode/solution in interface, respectively. The *Q* represents the electrode double-layer capacitance which formed at electrode/solution interface. The corresponding parameters of R_{ct} are exhibited in Table 3. Accordingly, we can see that the DIA of these four kinds of electrocatalysts are arranged in the following order: Pt (5537 Ω cm^2) > Pt_3Ni (1317 Ω cm^2) > $Pt/MoS_2/RGO$ (320.0 Ω cm^2) > $Pt_3Ni/MoS_2/RGO$ (156.2 Ω cm^2). This is also consistent with the above-mentioned remarkable catalyst performance.

Apart from the catalytic activity, the long-term stability of catalysts is another crucial factor for evaluating their practical applications. To investigate the long-term stability of the as-prepared samples toward the oxidation of ethylene glycol, the CVs of 150 cycles have been measured on the different catalysts modified electrodes in 1.0 M EG + 1.0 M KOH solution. Fig. 7 shows the forward peak current densities of EGOR in the scan *vs.* the CVs cycle number. Firstly, as can be seen from Fig. 7A, although the current density of Pt_3Ni reached 685 mA mg_{Pt}^{-1} at the beginning, the current density decreased continuously in the later stages, suggesting that the Pt_3Ni was readily poisoned by CO and other reaction intermediates generated *via* incomplete oxidation of ethylene glycol. Moreover, compared with $Pt/MoS_2/RGO$ electrode, $Pt_3Ni/MoS_2/RGO$ electrode revealed higher catalytic activity and stability, the maximum current density of $Pt_3Ni/MoS_2/RGO$ electrode reaches to 2062 mA mg_{Pt}^{-1} In addition, after 150 cycles, the peak current density of $Pt_3Ni/MoS_2/RGO$ electrode reduces by 5.32%, while $Pt/MoS_2/RGO$ electrode reduces about 41.6%. Meanwhile, the effect on the different molar ratio of Pt and Ni of $Pt_xNi/MoS_2/RGO$ catalysts on EGOR activity and stability is investigated. Fig. 7B shows that the optimum molar ratio of Pt and Ni in $Pt_xNi/MoS_2/RGO$ samples is 3:1. This result further proves that the $Pt_3Ni/MoS_2/RGO$ electrode has much higher electrocatalytic activity and better stability for EGOR than $PtNi/MoS_2/RGO$, $Pt_2Ni/MoS_2/RGO$ and $Pt_4Ni/MoS_2/RGO$ catalysts. From above results, we conclude that the appropriate addition with Ni content can enhance the electro-catalytic performance of $PtNi/MoS_2/RGO$ catalyst by changing Pt's electronic structure.

In order to further study the anti-poisoning abilities of the catalysts, the chronoamperometric (CA) curves and chronopotentiometry (CP) curves were evaluated. As shown from Fig. 8A, the CA curves show the change of current density in 1500 s at the potential of −0.2 V of different catalysts. It is obviously found that the current density decreased rapidly at the initial minute for all the catalysts. This may be caused by the formation of Pt oxides and CO-like intermediates on the surface of electrodes, which induces the partial poisoning of the catalysts during the process of EGOR reaction [51,52]. More important, in the entire experimental testing process, the $Pt_3Ni/MoS_2/RGO$ electrode exhibits a higher current density compared to the other catalysts, implying the superior poisoning-tolerance ability of $Pt_3Ni/MoS_2/RGO$ electrode than the others.

In addition, the CP experiment was also used to confirm the anti-poisoning abilities of the different catalysts and the results were shown in Fig. 8B. The potential enhances with the time going and then jumps to a higher potential eventually for all catalysts,

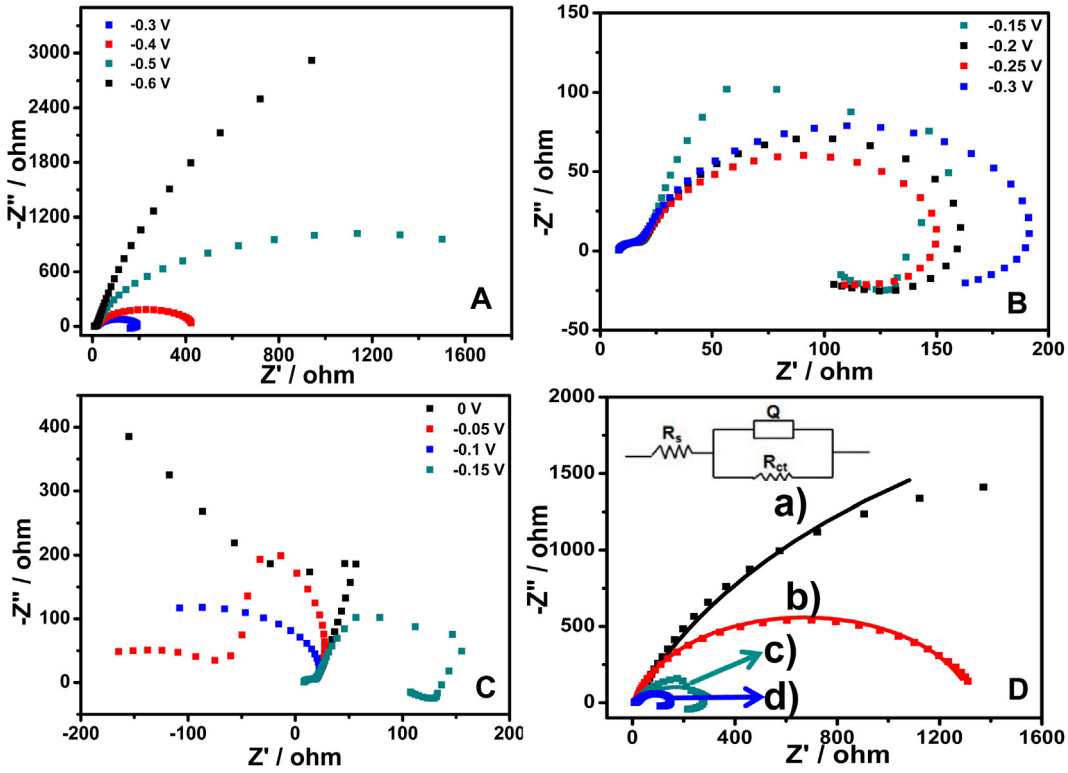

Fig. 6. (A–C) Nyquist plots of the $Pt_3Ni/MoS_2/RGO$ electrode in 1.0 M EG + 1.0 M KOH solution at the potentials from −0.60 V to 0 V. (D) Nyquist plots of Pt (a), Pt_3Ni (b), $Pt/MoS_2/RGO$ (c), and $Pt_3Ni/MoS_2/RGO$ (d) in 1.0 M EG + 1.0 M KOH solution at a potential of −0.25 V. The inset is a equivalent circuit to fit the impedance spectra.

Table 3
The parameters of *Rct* from equivalent circuits for different electrodes at EG Electrolyte.

Electrode	Pt	Pt_3Ni	$Pt/MoS_2/RGO$	$Pt_3Ni/MoS_2/RGO$
Ω cm^2	5537	1317	320.0	156.2

suggesting that the catalysts have been poisoned by intermediate poisonous species (such as CO_{ads}) [53]. It is clearly shown that the sustaining time of $Pt_3Ni/MoS_2/RGO$ is about 4021 s, which is much longer than Pt electrode (280.6 s), Pt_3Ni electrode (918.3 s) and $Pt/MoS_2/RGO$ electrode (1739 s), about 14.3, 4.40 and 2.30 times longer than Pt, Pt_3Ni and $Pt/MoS_2/RGO$, respectively. This result further confirms that the anti-poison ability of $Pt_3Ni/MoS_2/RGO$ electrode is better than others electrodes.

Additionally, CO stripping voltammetry was used to evaluate the catalytic activity and stability of Pt-based catalysts. As shown in Fig. 9, CO stripping CVs for Pt_3Ni, $Pt/MoS_2/RGO$ and $Pt_3Ni/MoS_2/RGO$ are exhibited. Firstly, a peak at ca. 0.7 V in the first positive scan (black line) was observed, which is attributed to CO stripping. With the desorption of CO, this peak disappears or reduces distinctly in the second positive scan. The values of catalysts' electrochemical active surface areas (ECSAs) were figured on the basis of the following Eq. (1):[54,55]

$$\mathrm{ECSA} = \frac{Q_{CO}}{[\mathrm{M}]\ 0.42\mathrm{mC\ cm^{-2}}} \quad (1)$$

Among Eq. (1), Q_{co} is the charge which is integral to the CO stripping CV; [M] means that the mass loading of Pt on the catalysts (about 8.0, 2.0, 1.9 μg for three catalysts); 0.42 mC cm^{-2} is the charge density attributed to the complete oxidation of CO monolayer. Secondly, the oxidation peak of CO for the $Pt_3Ni/MoS_2/RGO$ electrode is significantly larger than the peak of the Pt_3Ni and $Pt/MoS_2/RGO$ electrode. The calculated ECSA values for Pt_3Ni, $Pt/MoS_2/RGO$ and $Pt_3Ni/MoS_2/RGO$ were 14.9, 55.5, 157 $cm^2\ mg_{pt}^{-1}$, respectively. Moreover, the CO stripping peak in the $Pt_3Ni/MoS_2/RGO$ samples was much larger than these of Pt_3Ni and $Pt/MoS_2/RGO$, which is also match well with the tendency of the value of ECSA. These phenomena indicate that the sample of $Pt_3Ni/MoS_2/RGO$ has more catalytic active sites, which is beneficial to EGOR.

We used XPS to further confirm the stability of MoS_2 in the as-prepared $Pt_3Ni/MoS_2/RGO$ electrocatalyst after EGOR. As illustrated in Fig. 10, a typical peak located at 229.0 and 232.3 eV are assigned to Mo $3d_{5/2}$ and Mo $3d_{3/2}$, respectively, and two peaks at 162.1 and 163.7 eV attributed to S $2p_{3/2}$ and S $2p_{1/2}$, respectively. These results are consistent with the XPS results of MoS_2 in $Pt_3Ni/MoS_2/RGO$ before the electrocatalytic oxidation of EG, indicating that the MoS_2 species were not oxidized during reaction.

Based on above discussion, the as-prepared $Pt_3Ni/MoS_2/RGO$ composites showed a promising prospect for the oxidation of EG in alkaline medium. The probable electrooxidation mechanism of EG was proposed as following. Firstly, with the 2D nanosheets of MoS_2 and RGO, the as-prepared Pt_3Ni nanoparticles were

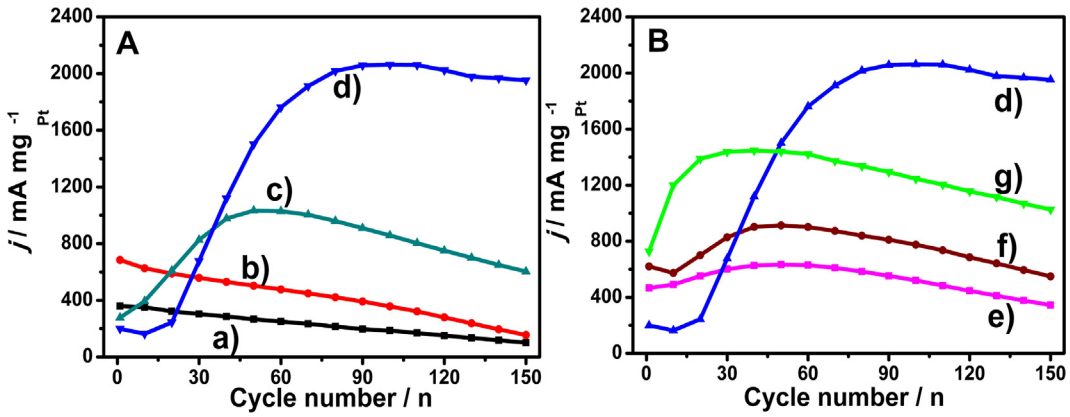

Fig. 7. (A) The peak current intensity of EGOR in the forward scan on Pt (a), Pt_3Ni (b), $Pt/MoS_2/RGO$ (c) and $Pt_3Ni/MoS_2/RGO$ (d) modified electrodes *vs.* the CVs cycle number in 1.0 M EG + 1.0 M KOH solution. (B) The peak current intensity of EGOR in the forward scan on $Pt_3Ni/MoS_2/RGO$ (d), $PtNi/MoS_2/RGO$ (e), $Pt_2Ni/MoS_2/RGO$ (f), and $Pt_4Ni/MoS_2/RGO$ (g) modified electrodes *vs.* the CVs cycle number under the same condition.

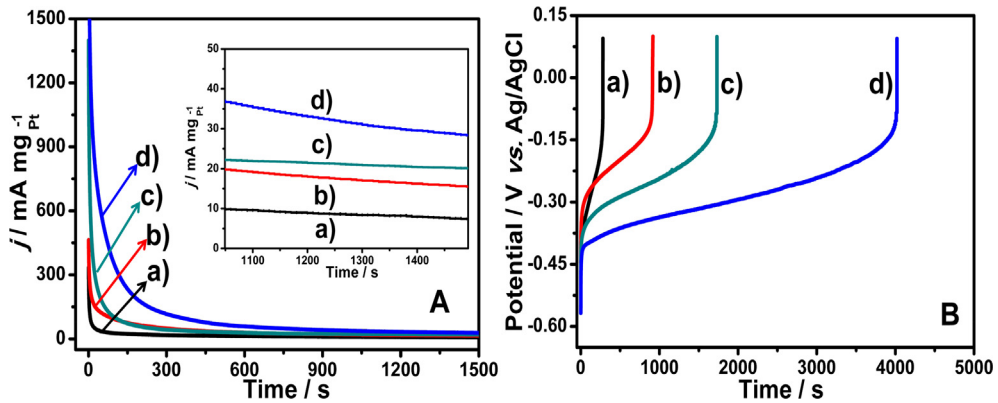

Fig. 8. Chronoamperometry curves (A) at −0.2 V (*vs.* Ag/AgCl) and chronopotentiometry curves (B) at 100 μA of Pt (a), Pt_3Ni (b), $Pt/MoS_2/RGO$ (c), and $Pt_3Ni/MoS_2/RGO$ (d) electrodes in 1.0 M EG + 1.0 M KOH solution.

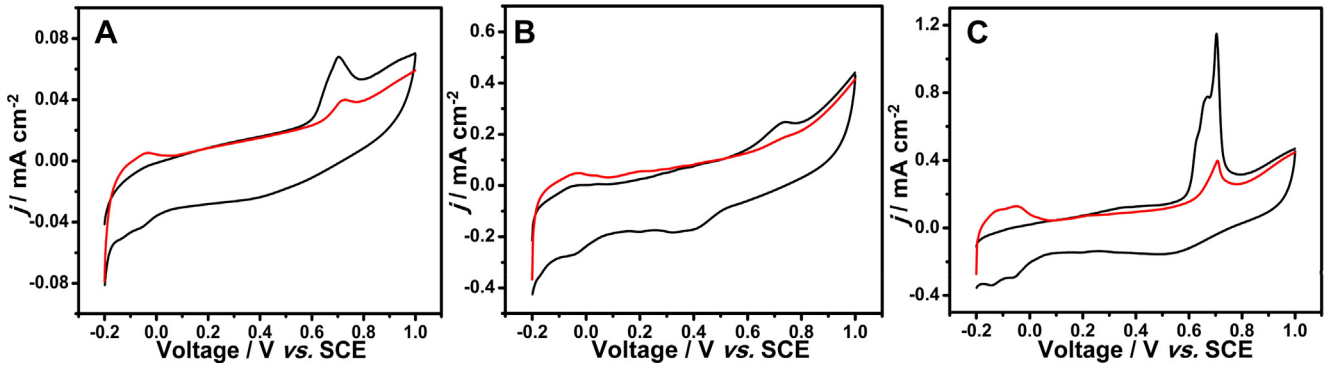

Fig. 9. CO-stripping voltammetry for Pt_3Ni (A), $Pt/MoS_2/RGO$ (B) and $Pt_3Ni/MoS_2/RGO$ (C) electrodes at 50 mV s^{-1} in H_2SO_4 solution.

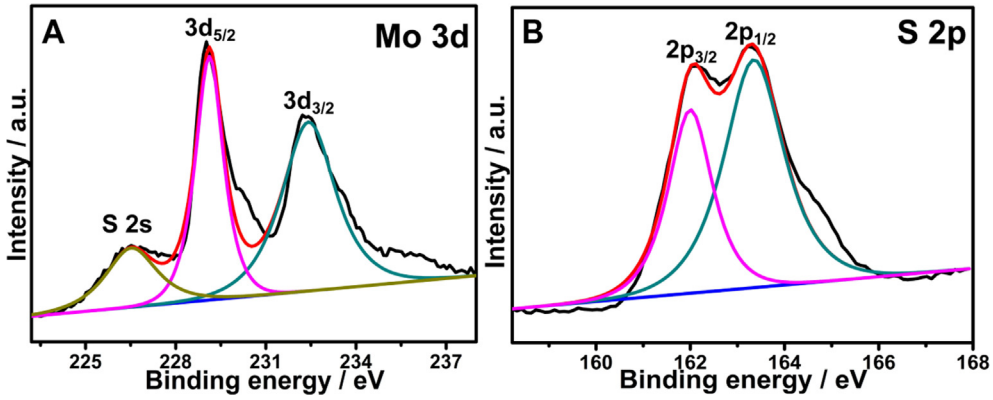

Fig. 10. XPS spectra of Mo 3d (A) and S 2p (B) of the MoS_2 in sample of $Pt_3Ni/MoS_2/RGO$ after EGOR.

well-dispersed on the surface of MoS_2/RGO nanosheets. Secondly, high electronic transport property of RGO contributes to fast electron transport during the EG oxidation reaction. Thirdly, in the direct ethylene glycol fuel cells, NiPt nanoparticles were deposited on the surface of MoS_2/RGO, which were acted as the active sites and the EG molecules were electro-oxidized to CO_2 on its surface. Owing to the synergistic effect between Ni and Pt atoms, the catalytic performances of EG oxidation were improved after the introduced Ni atom in the metallic PtNi. The main steps for the oxidation of EG were described as follow equations: [10,13,56]

$$(CH_2OH)_{2(solution)} \rightarrow Pt{-}(CH_2OH)_{2(ads)} \quad (2)$$

$$Pt{-}(CH_2OH)_{2(ads)} + 2OH^- \rightarrow Pt\text{-}(:COH)_2 + 2H_2O + 2e^- \quad (3)$$

$$Pt\text{-}(:COH) + 2OH^- \rightarrow Pt\text{-}HCOO_{(ads)} + H_2O + 2e^- \quad (4)$$

$$Pt{-}HCOO_{(ads)} + e^- \rightarrow Pt{-}CO_{ads} + OH^- \quad (5)$$

$$Pt + OH^- \rightarrow Pt{-}OH_{(ads)} + e^- \quad (6)$$

$$Pt{-}CO_{(ads)} + Pt{-}OH_{(ads)} \rightarrow CO_2 + 2Pt + H^+ + e^- \quad (7)$$

$$Ni + OH{-}\rightarrow Ni{-}OH_{(ads)} + e^- \quad (8)$$

$$Pt{-}CO_{(ads)} + Ni{-}OH_{(ads)} \rightarrow CO_2 + Pt + Ni + H^+ + e^- \quad (9)$$

4. Conclusion

In summary, 2D MoS_2/RGO composites were synthesized and then used as an effective support for the deposition of Pt_xNi alloy electrocatalysts. The as-prepared $Pt_xNi/MoS_2/RGO$ modified electrode shows remarkably enhanced electrocatalytic activity and stability in ethylene glycol oxidation process compared with $Pt/MoS_2/RGO$ electrode. In addition, compared with different molar ratio of Pt and Ni alloy, the as-prepared $Pt_3Ni/MoS_2/RGO$ modified electrode displays more prominent catalytic performance for the EGOR. These results indicate that the as-prepared $Pt_3Ni/MoS_2/RGO$ modified electrode can provide more insights for the wider application of the direct ethylene glycol fuel cell system.

Acknowledgment

We appreciate the support of the National Natural Science Foundation of China (Grant 21603111, 51702173). This work was also sponsored by K. C. Wong Magna Fund in Ningbo University.

References

[1] S. Giddey, S.P.S. Badwal, A. Kulkarni, C. Munnings, A comprehensive review of direct carbon fuel cell technology, Prog. Energ. Combust. 38 (2012) 360–399.
[2] Q. Lin, Y. Wei, W. Liu, Y. Yu, J. Hu, Electrocatalytic oxidation of ethylene glycol and glycerol on nickel ion implanted-modified indium tin oxide electrode, Int. J. Hydrogen Energ. 42 (2017) 1403–1411.
[3] A.S. Arico, S. Srinivasan, V. Antonucci, DMFCs: from fundamental aspects to technology development, Fuel Cells 1 (2001) 133–161.
[4] B. Zheng, T. Ouyang, Z. Wang, J. Long, Y. Chen, Z. Liu, Enhanced plasmon-driven photoelectrocatalytic methanol oxidation on Au decorated a-Fe_2O_3 nanotube arrays, Chem. Commun. 54 (2018) 9583–9586.
[5] T. Ouyang, Y. Ye, C. Wu, K. Xiao, Z. Liu, Heterostructures composed of N-doped carbon nanotubes encapsulating cobalt and b-Mo_2C nanoparticles as bifunctional electrodes for water splitting, Angew. Chem. Int. Ed. 58 (2019) 4923–4928.
[6] J. Wang, T. Ouyang, N. Li, T. Ma, Z. Liu, S, N co-doped carbon nanotube-encapsulated core-shelled CoS_2 @Co nanoparticles: efficient and stable bifunctional catalysts for overall water splitting, Sci. Bull. 63 (2018) 1130–1140.

[7] H. Cheng, M. Li, C. Su, N. Li, Z. Liu, Cu-Co bimetallic oxide quantum dot decorated nitrogen-doped carbon nanotubes: a high-efficiency bifunctional oxygen electrode for Zn-air batteries, Adv. Funct. Mater. 27 (2017) 1701833.
[8] E. Antolini, E.R. Gonzalez, Alkaline direct alcohol fuel cells, J. Power Sources 195 (2010) 3431–3450.
[9] H. Wu, A review of recent development: transport and performance modeling of PEM fuel cells, Appl. Energy 165 (2016) 81–106.
[10] A. Serov, C. Kwak, Recent achievements in direct ethylene glycol fuel cells (DEGFC), Appl. Catal. B: Environ. 97 (2010) 1–12.
[11] L. An, R. Chen, Recent progress in alkaline direct ethylene glycol fuel cells for sustainable energy production, J. Power Sources 329 (2016) 484–501.
[12] V. Livshits, E. Peled, Progress in the development of a high-power, direct ethylene glycol fuel cell (DEGFC), J. Power Sources 161 (2006) 1187–1191.
[13] H. Yue, Y. Zhao, X. Ma, J. Gong, Ethylene glycol: properties, synthesis, and applications, Chem. Soc. Rev. 41 (2012) 4218–4244.
[14] H.J. Kim, S.M. Choi, S. Green, G.A. Tompsett, S.H. Lee, G.W. Huber, W.B. Kim, Highly active and stable PtRuSn/C catalyst for electrooxidations of ethylene glycol and glycerol, Appl. Catal. B: Environ. 101 (2011) 366–375.
[15] V. Livshits, M. Philosoph, E. Peled, Direct ethylene glycol fuel-cell stack—study of oxidation intermediate products, J. Power Sources 178 (2008) 687–691.
[16] N. Ji, T. Zhang, M. Zheng, A. Wang, H. Wang, X. Wang, J. Chen, Direct catalytic conversion of cellulose into ethylene glycol using nickel-promoted tungsten carbide catalysts, Angew. Chem. Int. Ed. 47 (2008) 8510–8513.
[17] Y. Liu, C. Luo, H. Liu, Tungsten trioxide promoted selective conversion of cellulose into propylene glycol and ethylene glycol on a ruthenium catalyst, Angew. Chem. Int. Ed. 51 (2012) 3249–3253.
[18] M. Zheng, A. Wang, N. Ji, J. Pang, X. Wang, T. Zhang, Transition metal-tungsten Bimetallic catalysts for the conversion of cellulose into ethylene glycol, ChemSusChem 3 (2010) 63–66.
[19] M. Xu, T. Liang, M. Shi, H. Chen, Graphene-like two-dimensional materials, Chem. Rev. 113 (2013) 3766–3798.
[20] K. Vignarooban, J. Lin, A. Arvay, S. Kolli, I. Kruusenberg, K. Tammeveski, L. Munukutla, A.M. Kannan, Nano-electrocatalyst materials for low temperature fuel cells: a review, Chin. J. Catal. 36 (2015) 458–472.
[21] V. Georgakilas, J.N. Tiwari, K.C. Kemp, J.A. Perman, A.B. Bourlinos, K.S. Kim, R. Zboril, Noncovalent functionalization of graphene and graphene oxide for energy materials, biosensing, catalytic, and biomedical applications, Chem. Rev. 116 (2016) 5464–5519.
[22] H. Jin, C. Guo, X. Liu, J. Liu, A. Vasileff, Y. Jiao, Y. Zheng, S. Qiao, Emerging two-dimensional nanomaterials for electrocatalysis, Chem. Rev. 118 (2018) 6337–6408.
[23] X.Y. Chia, A.Y.S. Eng, A. Ambrosi, S.M. Tan, M. Pumera, Electrochemistry of nanostructured layered transition-metal dichalcogenides, Chem. Rev. 115 (2015) 11941–11966.
[24] C. Zhai, M. Zhu, D. Bin, F. Ren, C. Wang, P. Yang, Y. Du, Two dimensional MoS_2/graphene composites as promising supports for Pt electrocatalysts towards methanol oxidation, J. Power Sources 275 (2015) 483–488.
[25] W. Yu, M.D. Porosoff, J. Chen, Review of Pt-based bimetallic catalysis: from model surfaces to supported catalysts, Chem. Rev. 112 (2012) 5780–5817.
[26] H. Huang, X. Wang, Recent progress on carbon-based support materials for electrocatalysts of direct methanol fuel cells, J. Mater. Chem. A 2 (2014) 6266–6291.
[27] Y. Wang, N. Zhao, B. Fang, H. Li, X. Bi, H. Wang, Carbon-supported Pt-based alloy electrocatalysts for the oxygen reduction reaction in polymer electrolyte membrane fuel cells: particle size, shape, and composition manipulation and their impact to activity, Chem. Rev. 115 (2015) 3433–3467.
[28] T. Xia, J. Liu, S. Wang, C. Wang, Y. Sun, L. Gu, R. Wang, Enhanced catalytic activities of NiPt truncated octahedral nanoparticles toward ethylene glycol oxidation and oxygen reduction in alkaline electrolyte, ACS Appl. Mater. Interf 8 (2016) 10841–10849.
[29] N. Travitsky, L. Burstein, Y. Rosenberg, E. Peled, Effect of methanol, ethylene glycol and their oxidation by-products on the activity of Pt-based oxygen-reduction catalysts, J. Power Sources 194 (2009) 161–167.
[30] L. Liu, G. Samjeské, S. Takao, K. Nagasawa, Y. Iwasawa, Fabrication of PtCu and PtNiCu multi-nanorods with enhanced catalytic oxygen reduction activities, J. Power Sources 153 (2014) 1–8.
[31] X. Weng, Q. Liu, J. Feng, J. Yuan, A. Wang, Dendrite-like PtAg alloyed nanocrystals: highly active and durable advanced electrocatalysts for oxygen reduction and ethylene glycol oxidation reactions, J. Colloid Interf. Sci. 504 (2017) 680–687.
[32] Z. Yu, Z. Zhang, Z. Lv, M. Liu, L. Zhang, A. Wang, L. Jiang, J. Feng, $Platinum_{69}$-$cobalt_{31}$ alloyed nanosheet nanoassemblies as advanced bifunctional electrocatalysts for boosting ethylene glycol oxidation and oxygen reduction, J. Colloid Interf. Sci. 525 (2018) 216–224.
[33] C. Zhai, M. Sun, M. Zhu, K. Zhang, Y. Du, Insights into photo-activated electrode for boosting electrocatalytic methanol oxidation based on ultrathin MoS_2 nanosheets enwrapped CdS nanowires, Int. J. Hydrogen Energ. 42 (2017) 5006–5015.
[34] C. Wang, J. Zhu, S. Liang, H. Bi, Q. Han, X. Liu, X. Wang, Reduced graphene oxide decorated with CuO-ZnO hetero-junctions: towards high selective gas-sensing property to acetone, J. Mater. Chem. A 2 (2014) 18635–18643.
[35] M. Zhu, C. Zhai, M. Sun, Y. Hu, B. Yan, Y. Du, Ultrathin graphitic C_3N_4 nanosheet as a promising visible-light-activated support for boosting photoelectrocatalytic methanol oxidation, Appl. Catal. B: Environ. 203 (2017) 108–115.
[36] K. Ding, Y. Zhao, L. Liu, Y. Cao, Q. Wang, H. Gu, X. Yan, Z. Guo, Pt-Ni bimetallic composite nanocatalysts prepared by using multi-walled carbon nanotubes as reductants for ethanol oxidation reaction, Int. J. Hydrogen Energ. 39 (2014) 17622–17633.
[37] A.M. Huízar-Félix, R. Cruz-Silva, J.M. Barandiarán, D.I. García-Gutiérrez, I. Orue, D. Merida, S. Sepúlveda-Guzmán, Magnetic properties of thermally reduced graphene oxide decorated with PtNi nanoparticles, J. Alloys Compd. 678 (2016) 541–548.
[38] P. Song, J. Feng, S. Zhong, S. Huang, J. Chen, A. Wang, Facile preparation of reduced graphene oxide supported PtNi alloyed nanosnowflakes with highly catalytic activity, RSC Adv. 5 (2015) 35551–35557.
[39] M. Cheng, X. Zhang, M. Wang, H. Huang, J. Ma, A facile electrochemical sensor based on well-dispersed graphene-molybdenum disulfide modified electrode for highly sensitive detection of dopamine, J. Electroanal. Chem. 768 (2017) 1–7.
[40] S.C. Zignani, V. Baglio, D. Sebastián, T.A. Rocha, E.R. Gonzalez, A.S. Aricò, Investigation of PtNi/C as methanol tolerant electrocatalyst for the oxygen reduction reaction, J. Electroanal. Chem. 763 (2016) 10–17.
[41] S. Shen, T. Zhao, J. Xu, Y. Li, Synthesis of PdNi catalysts for the oxidation of ethanol in alkaline direct ethanol fuel cells, J. Power Sources 195 (2010) 1001–1006.
[42] X. Gao, Y. Wang, H. Xie, T. Liu, W. Chu, High activity of a Pt decorated Ni/C nanocatalyst for hydrogen oxidation, Chin. J. Catal. 38 (2017) 396–403.
[43] S. Lee, H. Kim, S. Choi, M. Seo, W. Kim, The promotional effect of Ni on bimetallic PtNi/C catalysts for glycerol electrooxidation, Appl. Catal. A: Gen. 429–430 (2012) 39–47.
[44] L. Liu, X. Lin, S. Zou, A. Wang, Ji. Chen, J. Feng, One-pot wet-chemical synthesis of PtPd@Pt nanocrystals supported on reduced graphene oxide with highly electrocatalytic performance for ethylene glycol oxidation, Electrochim. Acta 187 (2016) 576–583.
[45] K. Ju, L. Liu, J. Feng, Q. Zhang, J. Wei, A. Wang, Bio-directed one-pot synthesis of Pt-Pd alloyed nanoflowers supported on reduced graphene oxide with enhanced catalytic activity for ethylene glycol oxidation, Electrochim. Acta 188 (2016) 696–703.
[46] Z. Yang, L. Liu, A. Wang, J. Yuan, J. Feng, Q. Xu, Simple wet-chemical strategy for large-scaled synthesis of snowflake-like PdAu alloy nanostructures as effective electrocatalysts of ethanol and ethylene glycol oxidation, Int. J. Hydrogen Energ. 42 (2017) 2034–2044.
[47] D. Li, Y. He, J. Feng, Q. Zhang, L. Zhang, L. Wu, A. Wang, Facile synthesis of prickly platinum-palladium core-shell nanocrystals and their boosted electrocatalytic activity towards polyhydric alcohols oxidation and hydrogen evolution, J. Colloid Interf. Sci. 516 (2018) 476–483.
[48] Y. Yang, W. Wang, Y. Liu, F. Wang, Z. Zhang, Z. Lei, Carbon supported heterostructured Pd-Ag nanoparticle: highly active electrocatalyst for ethylene glycol oxidation, Int. J. Hydrogen Energ. 40 (2015) 2225–2230.
[49] Z. Bai, R. Huang, M. Shi, Q. Zhang, L. Yang, Z. Yang, J. Zhang, Novel Ag@C nanocables supported Pd anodes and its implication in energy conversion using direct liquid fuel cells, Appl. Energy 175 (2016) 429–434.
[50] Q. Liu, Y. Xu, A. Wang, J. Feng, Simple wet-chemical synthesis of core-shell Au-Pd@Pd nanocrystals and their improved electrocatalytic activity for ethylene glycol oxidation reaction, Int. J. Hydrogen Energ. 41 (2016) 2547–2553.
[51] M. Sun, J. Hu, C. Zhai, M. Zhu, J. Pan, A p-n heterojunction of CuI/TiO_2 with enhanced photoelectrocatalytic activity for methanol electro-oxidation, Electrochim. Acta 245 (2017) 10490–10498.
[52] C. Zhai, J. Hu, M. Sun, M. Zhu, Two dimensional visible-light-active Pt-BiOI photoelectrocatalyst for efficient ethanol oxidation reaction in alkaline media, Appl. Surf. Sci. 430 (2018) 578–584.
[53] R. Yue, Q. Zhang, C. Wang, Y. Du, P. Yang, J. Xu, Graphene-poly(5-aminoindole) composite film as Pt catalyst support for methanol electrooxidation in alkaline medium, Electrochim. Acta 107 (2013) 292–300.
[54] C. Zhai, J. Hu, M. Sun, M. Zhu, High-performance visible-light-driven Pt/CdS/graphene photoelectrocatalysts for methanol oxidation, Energy Technol. 5 (2017) 1292–1299.
[55] H. Qian, S. Chen, Fu. Yo, X. Wang, Platinume-palladium bimetallic nanoparticles on graphitic carbon nitride modified carbon black: a highly electroactive and durable catalyst for electrooxidation of alcohols, J. Power Sources 300 (2015) 41–48.
[56] F. Shao, J. Feng, Z. Yang, S. Chen, J. Yuan, A. Wang, Cytosine assisted aqueous synthesis of AgPt hollow alloyed nanostructures as highly active electrocatalyst for ethylene glycol oxidation and hydrogen evolution, Int. J. Hydrogen Energy 42 (2017) 24767–24775.